A multiscale survey of the “Buckle Gum”: Hydrostatic response of elastomers filled with hollow thermoplastic microspheres

Hugo Madeira, Lucas Tanné, Ivanna Pivdiablyk, Michel Coret, Pierre Rublon, Justine Papillon, Jérôme Adrien, Erwan Verron

Materials & Design 260 (2025) 115234

Contents lists available at ScienceDirect

Materials & Design

journal homepage: www.elsevier.com/locate/matdes

A multiscale survey of the "*Buckle Gum*": Hydrostatic response of elastomers filled with hollow thermoplastic microspheres

H. Madeira [a,*], L. Tanné [a,b], I. Pivdiablyk [a], M. Coret [a], P. Rublon [b], J. Papillon [c], J. Adrien [c], E. Verron [a]

[a] Nantes Université, Ecole Centrale de Nantes, CNRS, GeM, UMR 6183, F-44000 Nantes, France
[b] Naval Group, Technocampus Océan, Rue de l'Halbrane, 44340 Bouguenais, France
[c] Université Lyon 1, INSA Lyon, CNRS, MATEIS, UMR 5510, 69100 Villeurbanne, France

ARTICLE INFO

Keywords:
Elastomer matrix composite
Hollow thermoplastic microspheres
Hydrostatic compression
X-ray computed tomography (CT)
Pre- and post-buckling regimes

ABSTRACT

"*Buckle Gum*" refers to elastomer matrix composites filled with hollow thermoplastic microspheres (HTM). These particles are attracting particular attention for applications involving pressure, since they are capable of reversible deformation, unlike their glass counterparts usually used in syntactic foams. This work provides direct evidence of this deformation under *in situ* conditions, using an experimental hydrostatic compression set-up embedded in a tomograph. The HTMs buckle at a certain critical pressure, beyond which shrinkage and loss of sphericity are observed, characteristic of a post-buckling regime. The resulting volume change across the microsphere population appears independent of volume fraction up to 10 bars, and is predominantly governed by the response of the largest particles. This observation corroborates hydrostatic compression tests conducted on the composite, analysed using an alternative imaging technique. Upon return to ambient pressure, nearly all HTMs recover their initial shape and volume without exhibiting damage. Our inverse modelling approach, supported by both tomographic and macroscopic experiments, reproduces the microspheres response for pre- and post-buckling regimes thanks to two complementary model branches based on the Composite Spheres Assemblage theory. Even though they cannot yet be unified, they provide a consistent framework for future modelling investigations.

1. Introduction

Polymer syntactic foams are innovative materials that have been on the rise for a few decades now. Their range of application span many industrial sectors, where they offer significant enhancements: improved corrosion resistance in automotive parts, lighter structures in aeronautics, increased buoyancy for offshore purposes, and acoustic stealth for a variety of applications including medical and defense [1,2,3,4,5,6]. Most studies in the literature have primarily focused on hollow glass microspheres (HGM) particles. As the first ones incorporated into syntactic foams, they continue to be predominantly used, due to the maturity of their manufacturing process and the affordability of their raw materials [7,8]. The markedly higher stiffness of glass micro particles results in improved mechanical strength of the composite material. In this context, the mechanical behaviour of HGM composites has been extensively studied across various matrix materials and under different loading conditions [9,10]. Among these, uniaxial and hydrostatic compression have received particular attention, through numerous experimental investigations [9,11,12,13], supported by FE modelling [14,15,16]. These studies revealed that the fragile glass shells fail above a certain critical pressure, as observed *in situ* by X-ray tomography [9,17,18,19]. From a macroscopic point of view, this failure manifests as a densification plateau in the pressure–volume response once the critical pressure is reached [20,21]. The associated damage is irreversible and the material does not recover its original properties upon unloading to ambient pressure.

Recently, new types of micro-particles have emerged: hollow thermoplastic microspheres (HTM). These micro particles, whose leading manufacturer is Expancel®, are made from an isobutane-expanded tripolymer [22]. They are particularly relevant when embedded in an elastomer matrix, as their use contributes to weight reduction and resource efficiency – similarly to HGM [23]. Their distinct mechanical response sets them apart from their glass counterparts under severe conditions: where HGMs fail above a certain critical pressure, HTMs will

* Corresponding author.
E-mail address: hugo.madeira@ec-nantes.fr (H. Madeira).

https://doi.org/10.1016/j.matdes.2025.115234
Received 17 July 2025; Received in revised form 26 October 2025; Accepted 26 November 2025
Available online 28 November 2025

buckle. This complex phenomenon manifests as deformation of the spheres surface, according to pressure-dependent buckling modes [24,25,26]. This behaviour during pressurization, reportedly remaining unobserved *in-situ* for now, provides HTM a significant advantage: the microspheres can now undergo cyclic loading beyond their critical buckling pressure, without irreversible damage.

Within the elastomer matrix composite, or "*Buckle Gum*", this reversible behaviour has been observed in uniaxial tension, shear, as well as in uniaxial, confined and hydrostatic compression [27,28,29,30,31]. Constitutive models describing these materials remain scarce and generally fall into two categories. On the one hand, phenomenological models were developed for compressible elastomers, without specific consideration of HTM composites and the buckling phenomenon [32,33]. On the other hand, models integrating the buckling of spheres in a continuous (hyper-)elastic medium have been developed [34,35,36,37], and compared with experiments [38,39]. The main result indicates that the polydispersity in microsphere sizes, along with their potential interactions, pose significant challenges to a detailed understanding of buckling and the determination of the corresponding critical pressures [40,41]. Therefore, progress in modelling requires bridging the scales by relating the macroscopic pressure–volume response of the material to the buckling of individual microspheres.

In this article, we propose to reconcile these scales during a hydrostatic pressure cycle, thanks to an X-ray tomography set-up with *in situ* observation, as well as a custom test bench for macroscopic hydrostatic tests. As shown in Fig. 1, three steps are considered: the initial state before testing, the pressurization, and finally the return to ambient pressure. For each of these stages, the response is analysed at the individual microsphere level, for the collective HTM population, and for the composite material as a whole. Finally, thanks to the Composite Spheres Assemblage theory of Hashin [42] we present initial attempts to model the material response, focusing on pre- and post-buckling regimes and their contribution to the composite mechanical behaviour.

2. Experimental methods

2.1. Materials and samples

The materials are polyurethane elastomers filled with various volume fractions of hollow thermoplastic microspheres (HTM). The matrix is obtained by polymerization of toluene diisocyanate and polyester polyols monomers. The HTM are supplied by Expancel®, and their volume fractions specified by the formulator are 5, 10, 15, 20 and 25 %.

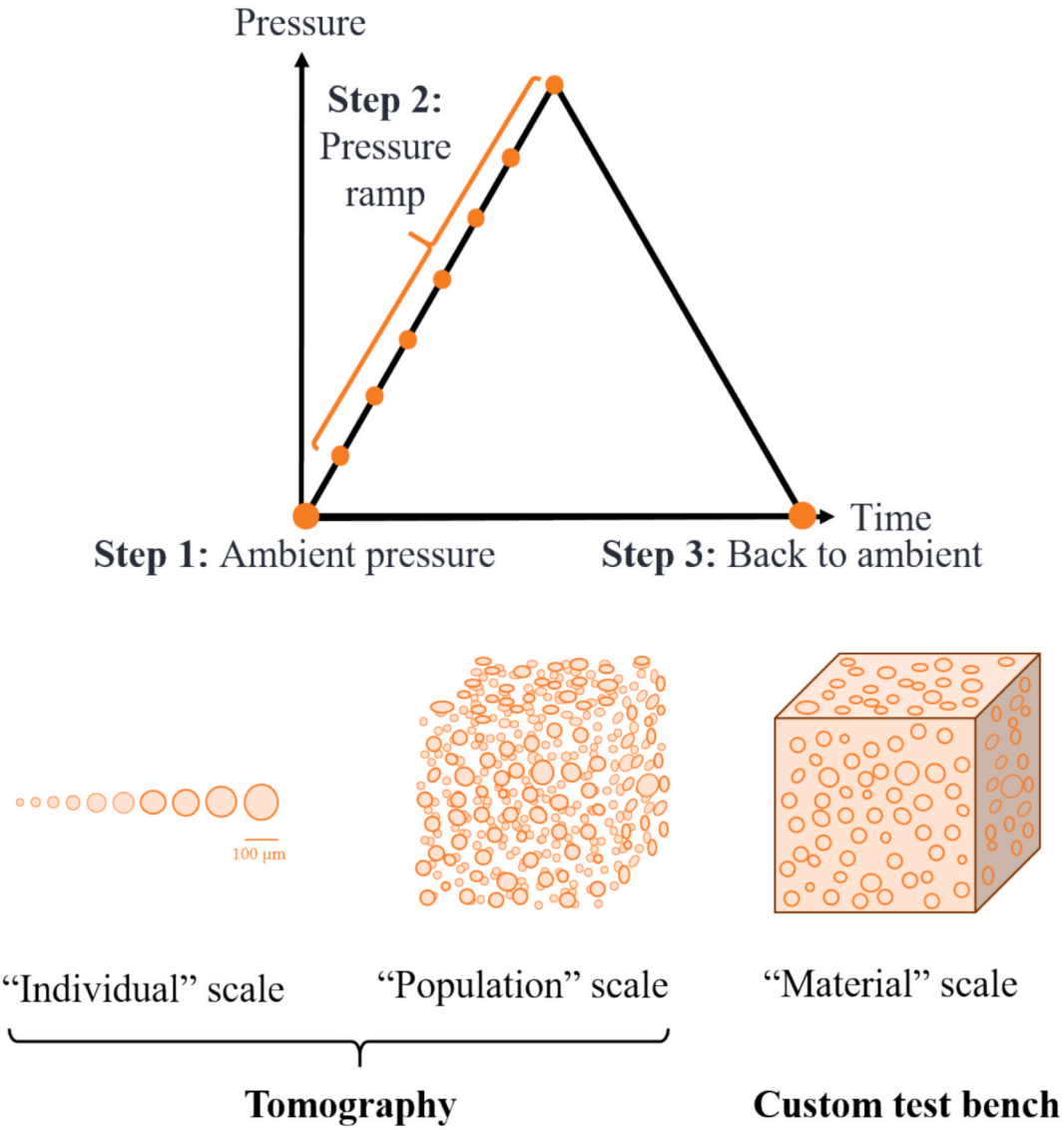

Fig. 1. Methodology to reconcile the material behaviour at all scales.

For simplicity, the materials will be named after the specified volume fractions, even though their effective volume fraction is determined subsequently.

2.2. X-ray micro tomography experimental setup and procedure

The experimental setup, shown in Fig. 2, is composed of a tailored mechanical testing machine directly embedded in an X-ray tomograph.

The mechanical part consists in exerting hydrostatic pressure on material cubes of 2 mm edge length. The samples are glued on a support in a water-filled chamber. By controlling the displacement of a translating motor, a piston compresses the water surrounding the elastomer, thus exerting an isotropic pressure measured by a sensor located at the top of the water column. This assembly is attached to the rotating table of the tomograph to image the samples volumes.

In situ volumetric microscopic observations are performed using a GE Phoenix v/tome/x s X-ray tomograph. Images are captured by 1200 projections within 360°, with a 3 μm^3 voxel size at 80 kV tube voltage. For these experimental parameters, the acquisition time lasts 15 min per pressure level. Exploitable pressure levels differ depending on the material HTM volume fraction; particularly extensive tests have been performed on the 20 %-filled material, up to 40 bars. Image analysis and post-processing are detailed in Appendix 1.

2.3. Properties at individual and population scales

Once the HTM are segmented, their volume is calculated from the volume of their constitutive voxels. The equivalent diameter $\varnothing_{eq}$ of a HTM follows the hypothesis of perfect spheres: it is the diameter of the sphere that has the same volume V,

$$\varnothing_{eq} = \sqrt[3]{\frac{6\,V}{\pi}}. \tag{1}$$

Uncertainties regarding the volume determination have been considered under the hypothesis that the uncertainty of voxel detection prevails over the voxel resolution one. An isotropic detection uncertainty of ± 0.5 vx has been chosen. Python package PyVista [43] has also been used for finely visualising the post-buckling of individual particles.

The distributions of properties among the particles population have been chosen to be volume-weighted, to lend weight to the larger microspheres, as the latter occupy a greater volume fraction. A complete derivation is documented in [41].

2.4. Density measurement

Materials' actual volume fractions were determined in a prior work [28].

2.5. Macroscopic hydrostatic experiments

Macroscopic hydrostatic experiments have been performed in a prior work with a custom experimental set-up [31]. It consists in a gas pressurization chamber fitted with a digital camera filming the samples. Images are then processed using 2D digital image correlation. The material being considered isotropic, the change in volume is measured during pressurization up to 8 bars. These results serve as comparison between properties at the "material" and "population" scales.

3. Results and discussion

This section is structured following the methodology depicted in Fig. 1. First, an initial characterization of the material at ambient pressure sets the ground for deeper analyses. Second, the behaviour of the material is examined at all scales, during pressurization. Finally, an observation back at ambient pressure allows for assessing reversibility.

3.1. Materials characterization at ambient pressure

The materials are first characterized under ambient pressure. While this section does not reveal any unusual findings, which are, however, consistent with observations reported in previous studies, it remains a necessary step prior to increasing the pressure.

3.1.1. "Individual" scale

Our investigations begin by imaging the microspheres in a sample of 20 % HTM material, placed in the tomograph before the apparatus is pressurized. The 26,544 microspheres of the sample useful area are segmented and sorted by increasing volume. Fig. 3 presents a 3D reconstruction of one individual per volume decile. The polydispersity of sphere sizes is particularly visible, as the smallest particles consist of only a few voxels, with volumes more than 1000 times smaller those of the largest ones.

3.1.2. "Population" scale

For the 20 % HTM material, Table 1 presents descriptive statistics of

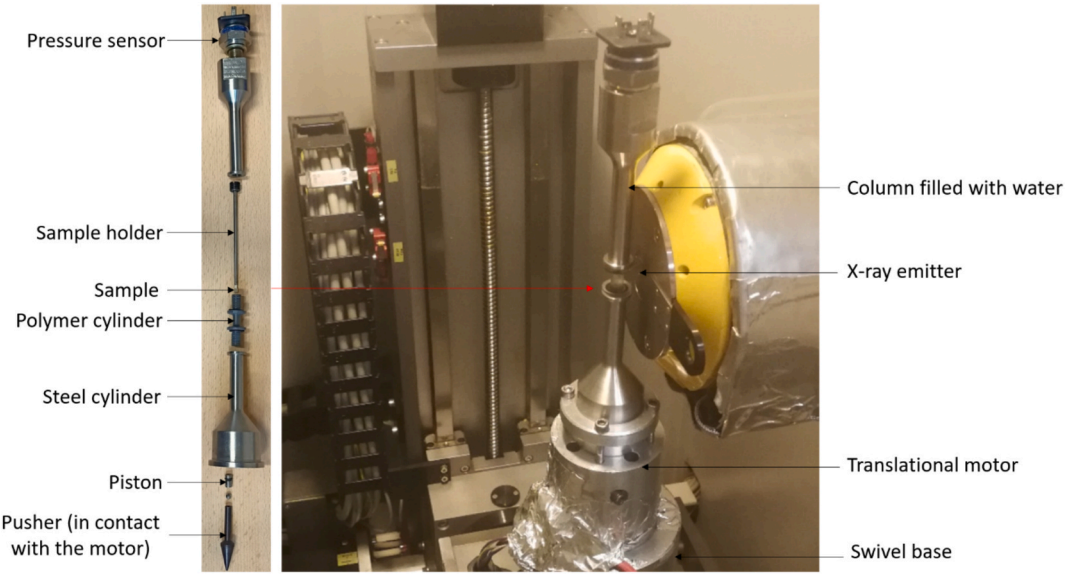

Fig. 2. In situ tomographic experimental setup.

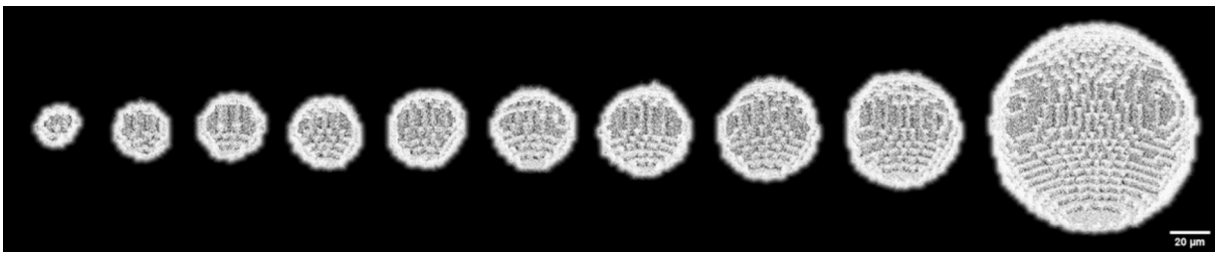

Fig. 3. An HTM individual representative from each decile of the 20 % HTM material.

Table 1
Descriptive statistics of microspheres volumes and diameters for the 20% HTM material.

	Minimum	1st quartile	Median	Mean	3rd quartile	Maximum
Volume V (µm^3)	513	19,521	36,396	55206.2	64,557	972,756
Diameter $\varnothing_{eq}$ (µm)	9.9	33.4	41.1	42.5	49.8	122.9

the equivalent volumes and diameters for this sample at ambient pressure. The particles median diameter, 41.1 µm, is close to the value specified by the HTM manufacturer (40 µm) determined by low angle laser light scattering [22]. The distribution of particles diameters can be found in Fig. 4a, where a histogram depicts the volume weighted occurrence frequencies inside 5 µm diameters ranges. The shape of the histogram and cumulative frequency curve indicate a normal distribution, which aligns with previous statistical investigations [27,41]. Parameters of a normal law are then fitted for each HTM volume fraction, and the corresponding distributions are plotted in Fig. 4b; it reveals that the volume fraction has a limited impact on the distribution parameters. Moreover, these results are in striking agreement with the ones of Curd et al. [41], although their HTM grade is slightly different.

3.1.3. *"Material" scale*

The actual volume fraction f_v of the materials were measured in [28]. The results are reported in Table 2. It is important to note that these measurements were performed on specimens significantly larger than those used for tomography (over 10^5 larger in volume). As such, they fully represent the volume fraction at the scale of an actual part, but may differ from the values obtained from smaller tomography samples. Overall, the measurements exhibit an acceptable repeatability, with values slightly lower to the nominal specifications. This minor discrepancy may arise from losses during the manufacturing process.

3.2. *Raising the pressure*

The behaviour of the HTM material during the pressure ramp is analysed with a particular attention paid to the individual scale, in order to investigate the buckling phenomenon. Subsequently, the analysis progresses to the population scale, and ultimately to the composite material as a whole.

Table 2
HTM volume fractions.

Specified volume fraction (%)	5	10	15	20	25
Volume fraction f_v (%)	4.6 ± 0.1	9.3 ± 0.3	13.5 ± 0.2	17.5 ± 0.1	23.2 ± 0.2

3.2.1. *"Individual" scale*

To visualise the effect of hydrostatic pressure on HTM, four individual microspheres from Fig. 3 are tracked during the pressure ramp. They are chosen to belong to four different deciles of the microsphere population, respectively 90–100 %, 70–80 %, 50–60 % and 20–30 %. Their morphological transformation is presented in Fig. 5 as a function of applied pressure. Qualitatively, a reduction of the particles size can be seen, as well as a clear change in shape.

To further explore this behaviour, light is shed on a single HTM: the one presented in Fig. 5a. The 3D surface of its constituent voxels is reconstructed using a hexagonal mesh via PyVista. In parallel, a volume-equivalent sphere is generated based on the particle voxel volume at ambient pressure, and centred on the microsphere centre of mass. Both representations are superimposed in Fig. 6. For each pressure level, the particle is colour-mapped according to the distance between its surface and the reference sphere at ambient pressure. While this distance is sensitive to the segmentation quality and the degree of smoothing applied during surface reconstruction, it remains sufficiently robust to observe deformation features. Readers are encouraged to refer to the

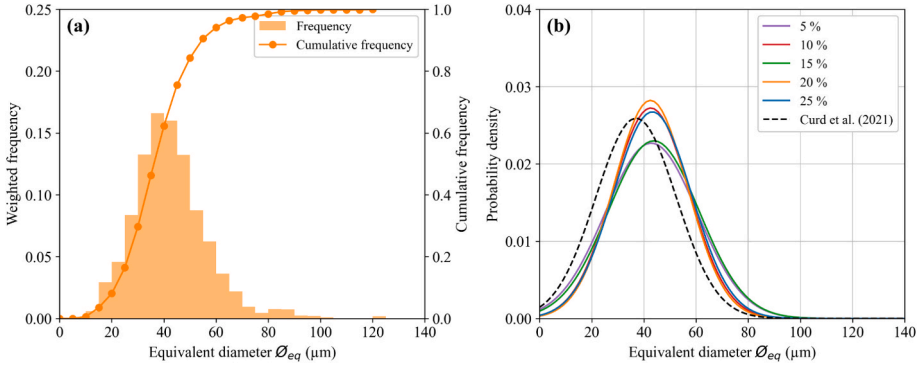

Fig. 4. (a) Equivalent diameter distribution for the 20 % HTM material. (b) Fitted normal distributions of equivalent diameter, for all volume fractions.

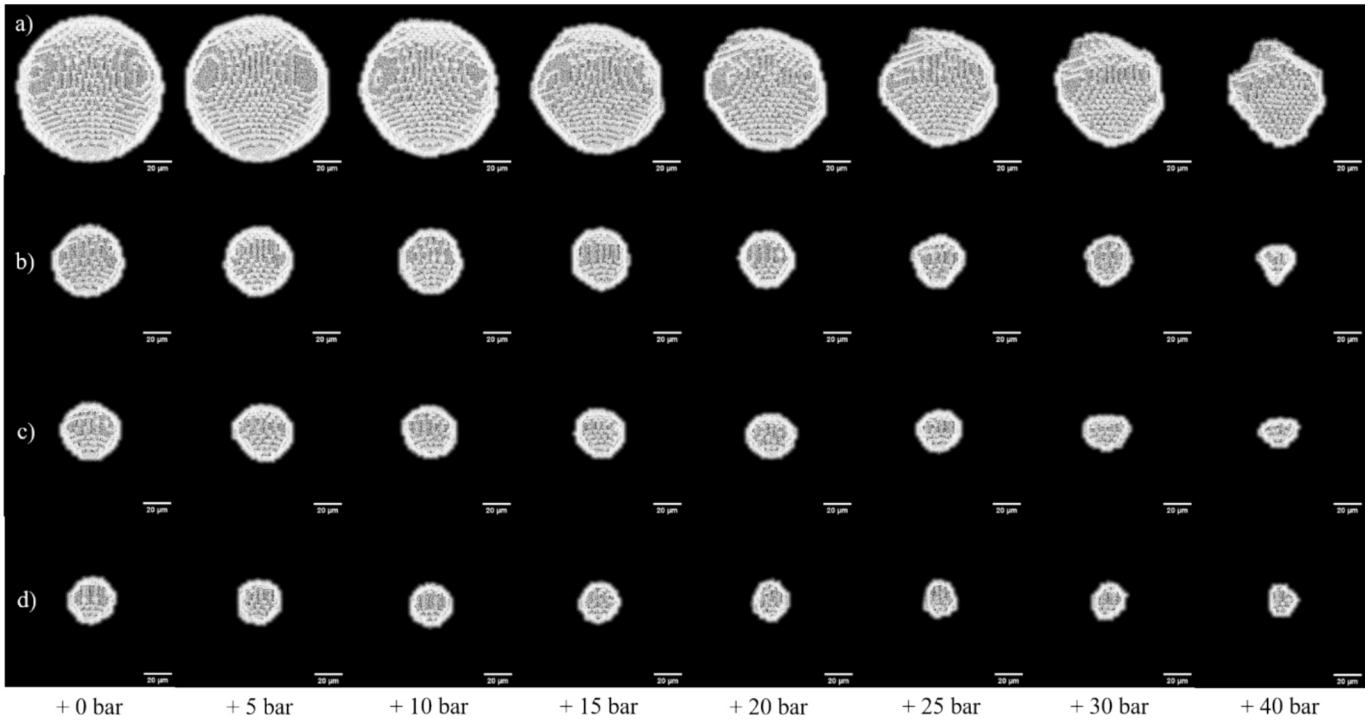

Fig. 5. HTM morphology during pressure ramp: an individual from (a) 90–100 %, (b) 70–80 %, (c) 50–60 % and (d) 20–30 % deciles of the 20 % HTM material.

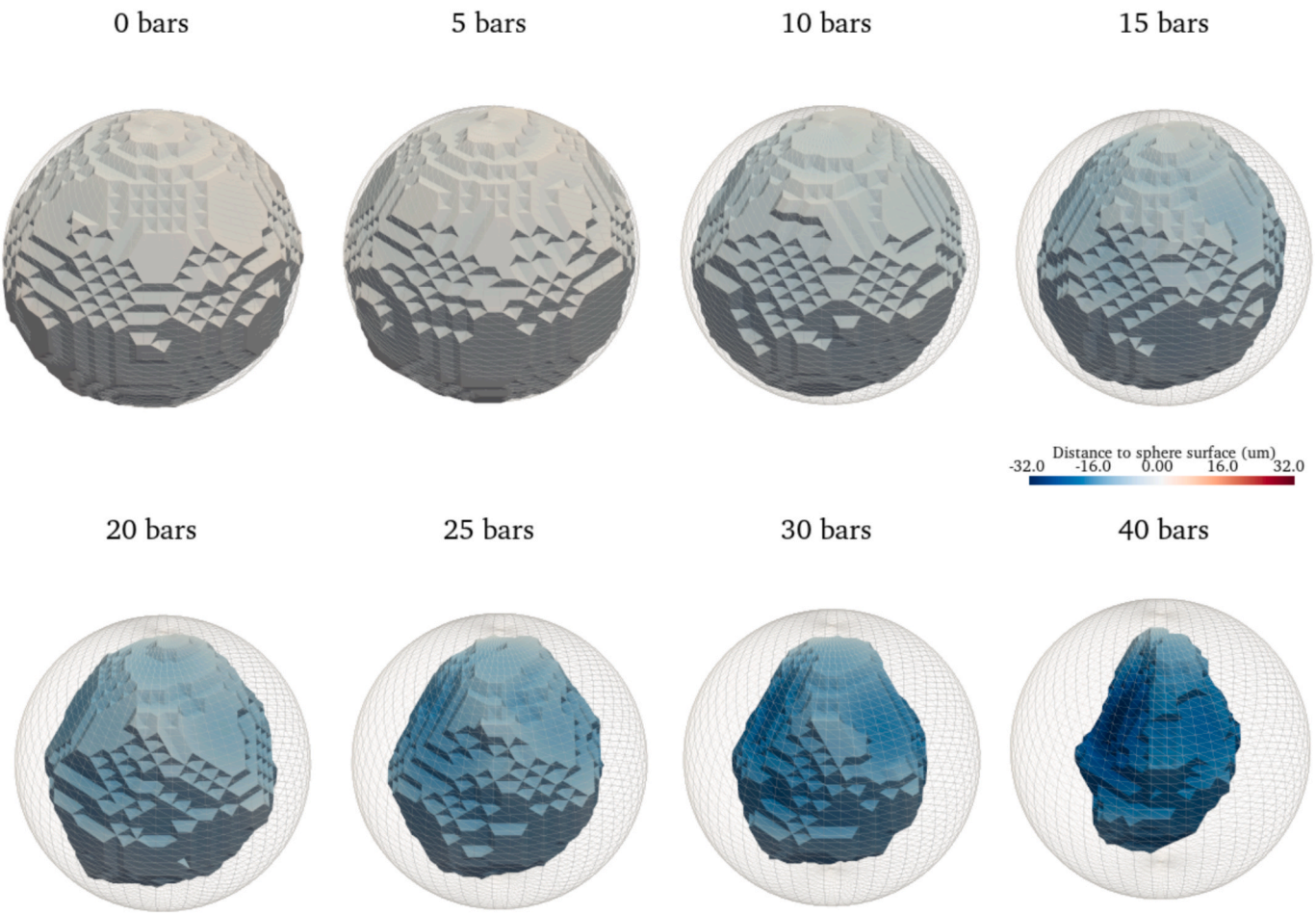

Fig. 6. Distance of particle reconstructed surface towards the reference equivalent sphere surface at ambient pressure, during the pressure ramp.

supplementary materials, which contain a 3D animated version of Fig. 6. In this version, the particles are rendered as hollow objects, offering a more realistic representation of HTM, in contrast to the filled rendering used in the paper to enhance visibility in 2D projections.

As pressure increases, the microsphere undergoes a gradual and non-uniform shrinkage, with its surface progressively deviating from the reference sphere. The deformation is significant, with the volume decreasing by over 75 % at 40 bars. Moreover, under pressure, the shape of the microsphere deviates from the perfect sphere, as shown in Fig. 7, where this time the reconstructed sphere maintains the same volume as the microsphere throughout the pressure ramp. A 3D animated version of Fig. 7 is also provided in supplementary materials.

To the best of our knowledge, this represents the first in situ observation of HTM deformation in such a material. Yet, can it truly be identified as buckling?

To try answering this, we propose to consider the work of Fok & Allwright [34]. Based on an energy method with a Rayleigh-Ritz trial function, they derived the critical pressure at which the buckling of a sphere takes place,

$$p(X,n) = \frac{2E_s}{3}\left(\frac{1+\nu_m}{1-\nu_m}\right)\left(1+\frac{E_m(1-\nu_s)}{E_s X(1+\nu_m)}\right)\left(p_1(n)X^3+p_2(n)X^2+p_3(n)\right), \quad (2)$$

connecting the microsphere thickness/mean radius ratio X, Young modulus E_m, E_s and Poisson ratios ν_m and ν_s, respectively of the matrix and the shell, the buckling mode n, and the applied pressure p. The functions $p_1(n)$, $p_2(n)$ and $p_3(n)$ are defined as follows:

$$p_1(n) = \frac{n(n+1)-(1-\nu_s)}{12(1-\nu_s^2)}, \quad (3)$$

$$p_2(n) = \frac{2}{(n-1)(n+2)(1+\nu_s)}, \quad (4)$$

$$p_3(n) = \frac{E_m}{E_s}\frac{(2n^3-n^2+3n-2)-\nu_m(2n^3-3n^2+5n+2)}{(n-1)^2(n+2)(3n+2-2\nu_m(2n+1))(1+\nu_m)}. \quad (5)$$

Application of Eqs. (2)-(5) to the microsphere from Fig. 6 involves data from a precedent paper, and literature. Both matrix Young modulus E_m and Poisson ratio ν_m were determined in [28]. Although the shell thickness was not measured, studies on grades similar to the one investigated suggest a typical thickness of approximately 0.29 μm [23,39], with little dependence on particle size [41]. This facilitates the implementation, since the equivalent diameter $\varnothing_{eq}$ can be used directly instead of the ratio X. Microspheres Poisson's ratio ν_s and Young's modulus E_s have also been proposed in [41]. Table 3 summarizes the parameters values, their sources used for substitution into Eq. (2).

Buckling takes place when the minimum pressure, called critical

Table 3
Parameters values and sources.

Parameter	Value	Source
E_m	6.00 E6 Pa	[28]
ν_m	0.495	
E_s	1.83 E9 Pa	[41]
ν_s	0.24	

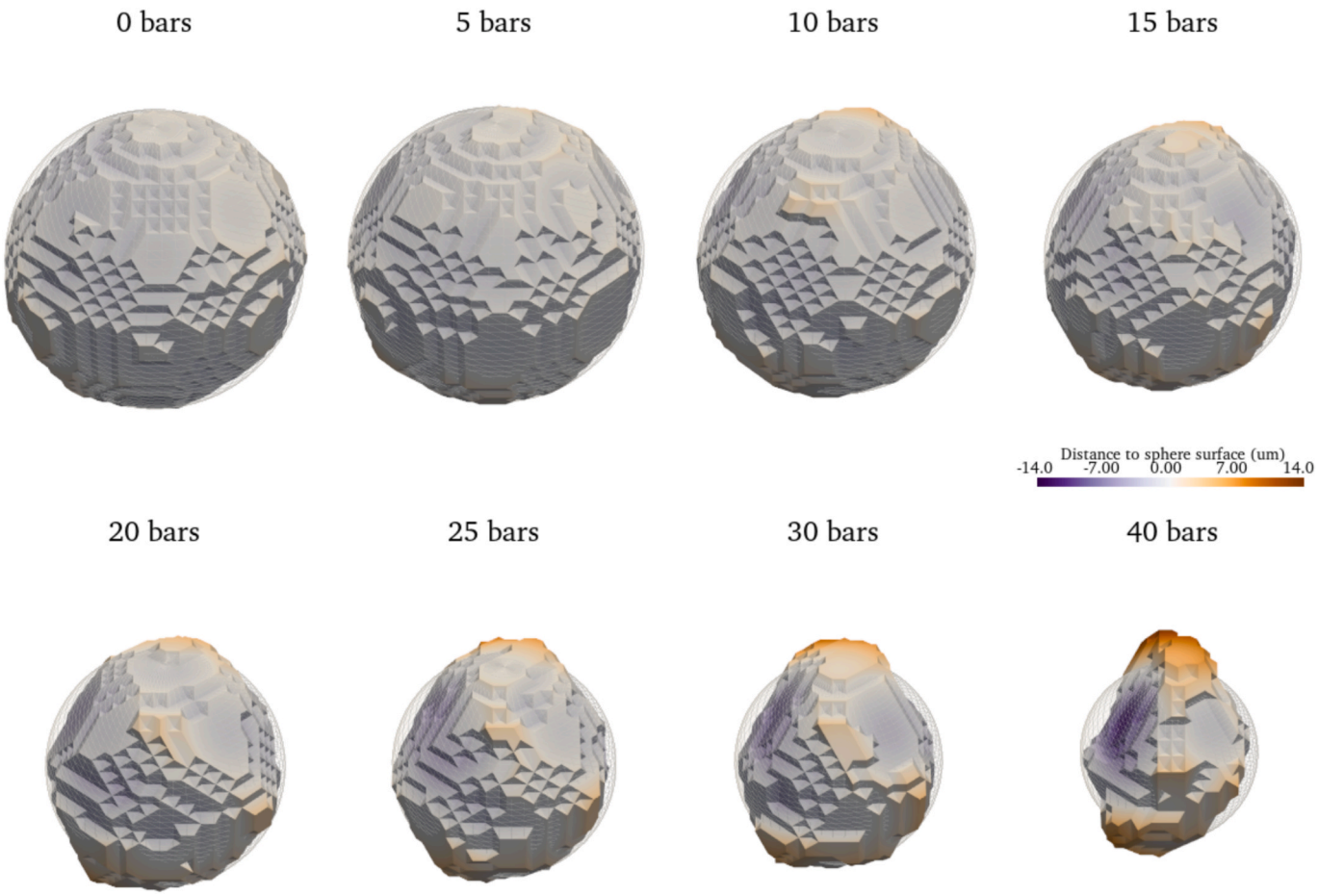

Fig. 7. Distance of particle reconstructed surface towards its own equivalent sphere surface, during the pressure ramp.

pressure p_c, defined as

$$p_c = \arg_p \left(\frac{\partial p}{\partial n} = 0 \right), \tag{6}$$

is reached. By plotting p_c as a function of $\varnothing_{eq}$ in Fig. 8, it is possible to relate the critical pressure and mode of a microsphere to its equivalent diameter. Since the predicted critical pressure and mode are sensitive to the shell thickness, we allowed it to vary, as commonly done in studies on syntactic foams [44,45,46,47]. Specifically, the thickness varies between 0.22 and 0.36, thus encompassing the standard deviation of the experimentally measured thickness reported by Curd et al. [41]. Critical pressure decreases with increasing microsphere diameter, whereas critical mode increases.

For the considered "Sphere a" from Fig. 6, we find a critical pressure of 4.2 bars, associated with mode n = 41. The thickness variation leads to a 20 % range in critical pressure, and a critical mode spanning from n = 35 to n = 55. This means that theoretically, the geoid at 5 bars in Fig. 6 has already undergone buckling, in a mode of high order implying the presence of about 20 wrinkles from pole to pole. As explained in the following remark, the resolution of the tomography is insufficient to clearly visualize such fine-scale deformation at this pressure.

Remark on the detectability of buckling patterns. Building upon Hutchinson and Koiter's work [25,48], the "*wavelengths are of the order of* $\Lambda = \sqrt{\varnothing_{eq} H/2}$ *and small compared with* $\varnothing_{eq}$ *for thin shells*", with H being the shell thickness. In our case, for the largest microsphere diameter and the smallest thickness (representing the most favourable scenario), the predicted buckling wavelength is $\Lambda = 4.27$ µm, which already violates the Shannon–Nyquist criterion, as our sampling wavelength is 3 µm ($> \Lambda/2$). More critically, resolving the buckling wrinkles would require a tomographic resolution finer than the wrinkle amplitude at the microsphere surface, referred to as the *deflection* in Hutchinson's work: "*much of the essential buckling behaviour of thin shells plays out in the range of deflections of the order of several shell thicknesses*" with amplitudes typically up to five times the shell thickness. Applied to our case, this corresponds to an approximative amplitude of 1.5 µm, for which our sampling wavelength again exceeds the Shannon–Nyquist limit.

For the smallest microspheres, as shown in Fig. 8, the critical buckling pressures are higher, and the corresponding buckling modes are of lower order, resulting in fewer but thicker wrinkles, which is favourable for visual observation of buckling onset. Unfortunately, due to their small size, these microspheres also fall below the effective resolution of the tomography. Therefore, our analysis is best focused on the largest microspheres, which offer the most favourable compromise between shrinkage visibility and imaging resolution.

As the pressure ramp progresses, increasingly pronounced surface wrinkling is observed in Fig. 6. In fact, for every pressure level above ambient pressure, the microsphere is already in a post-buckling state. Thus, we observe the *in situ* post-buckling response of an individual microsphere embedded in an elastomer matrix, a configuration that has

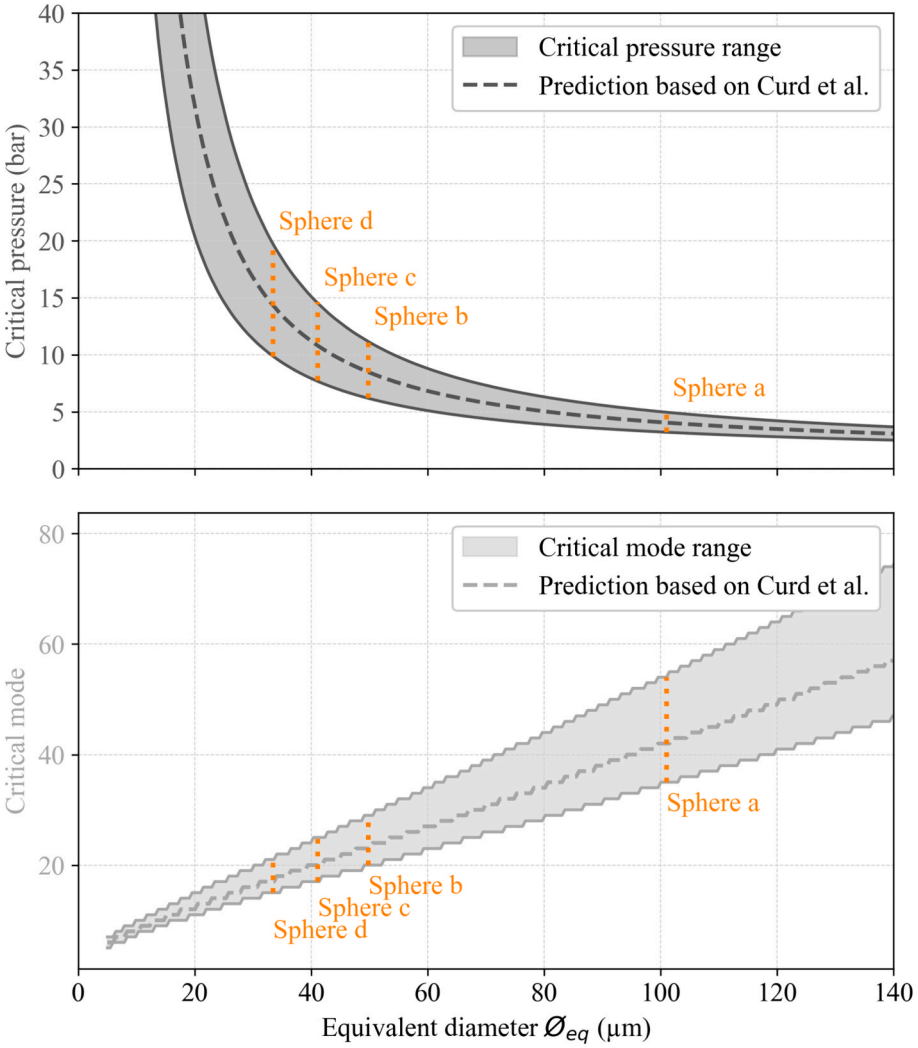

Fig. 8. Critical buckling pressure and mode associated with a given equivalent diameter.

rarely been explored. This regime is known to be highly complex, as transitions between different buckling modes can occur, leading to phenomena such as "cascades of buckling thresholds" or "snap buckling" [25,36,49]. Moreover, in this non-linear domain, the buckling mode is not uniquely defined for a given applied pressure. It is influenced by several factors, including the evolution of the microsphere natural curvature, the presence of shell imperfections, and interactions with neighbouring microspheres [25,26,40]. It is therefore not possible to establish a direct correspondence between the geoids in Fig. 6 and an ideal spherical mode; however, the post-buckling deformation can still be clearly visualized.

3.2.2. "Population" scale

In this section, the influence of pressure on diameter and volume change of the whole HTMs population is examined statistically. Then, building on the previous section, it is investigated whether all microspheres contribute equally to the properties of the population or if certain individuals dominate the overall response.

Pressure influence on microsphere size and shape.

The change in equivalent diameter $\varnothing_{eq}$ during the pressure ramp is examined for a single HTM rate of 20 %, shown in Fig. 9a. The diameter distribution is represented using box plots, with the box edges indicating the first and third quartiles, along with markers for the median and mean. All these indicators clearly show a decrease in $\varnothing_{eq}$ during the pressure ramp, which aligns with visual observations in Fig. 6. This decrease is accompanied by a narrowing of the interquartile range, thus concentrating the distribution around the median. Attention can be paid on the median diameter, while extending the scope to all HTM rates, as shown in Fig. 9b. The evolution of this characteristic with increasing pressure appears consistent across all formulations, suggesting that it is independent of the volume fraction up to 10 bars. As detailed in Appendix 2, regarding the microspheres shape, a plateau in sphericity is observed, with changes only above 15–20 bar while sphericity remains high, in accordance with Fig. 7.

Pressure influence on change in volume.

The volume ratio V/V_0 of the microsphere population is considered during the pressure ramp. For the 20 % HTM material, Fig. 10a shows a monotonic decrease in this ratio, explained by the loss of volume by shrinkage of the spheres. The intensity of this change is significant: it reaches less than 75 % of the initial volume, which is consistent with observations made in Fig. 6. This behaviour is clearly independent of the volume fraction up to 10 bars, as shown in Fig. 10b.

Nevertheless, Fig. 9 and Fig. 10 exhibit an inflection of the curve: there is a relatively slow variation at low pressures followed by an increasing slope, with a smooth transition. This behaviour evokes the post-buckling transition of spheres, beyond which the change in volume would intensify. As the transition appears to occur around 5 bars, which according to Fig. 8 corresponds to the magnitude of critical pressures for the largest microspheres encountered in this sample, a key question arises: do all the microspheres contribute equally to the changes in material properties under pressure, or do certain microspheres, particularly the largest ones, dictate the overall response?

Which microspheres drive the change in volume?

Respective contributions of each volume decile to microspheres total volume are examined throughout the pressure ramp. They are shown in Fig. 11, where each shade of orange corresponds to the volume proportion occupied by a decile. 10 % of the largest spheres represent 40 % of the volume; it rises to 87 % if the 50 % largest spheres are considered. These proportions are fairly stable as the sample is pressurized, although the contribution of the largest spheres decreases slightly at high pressure. Thus, the total change in volume appears to be primarily governed by the largest spheres in the sample.

To substantiate this observation, Fig. 12 reproduces Fig. 10a by isolating the respective contributions of each decile. The black curve replicates the global response from Fig. 10a, while the coloured curves corresponding to each decile are superimposed, allowing a direct comparison of their individual influences. The behaviour differs depending on the considered decile, as microspheres of small volumes have a less pronounced evolution than the larger ones. This is easily explained in light of the critical pressures exhibited in Fig. 8: the smaller the size of the spheres, the later the buckling occurs, resulting in a more gradual volume change. Conversely, as the microspheres size increases, the volume loss under pressure becomes more abrupt, with the response increasingly resembling the global curve: the largest spheres dictate the overall behaviour of the material. Nevertheless, the inflection observed in Fig. 9 and Fig. 10 can now be confidently attributed to the buckling of the larger microspheres. This transition is smooth because of the polydispersity of HTM sizes, whose critical buckling pressure is spread over a range of pressures.

Having understood the effects and implications of the transition from the pre-buckling to the post-buckling regime at the HTM population scale, we now aim to bridge the gap between the scales by comparing the previous results with mechanical tests conducted on the Buckle Gum.

3.2.3. "Material" scale

Results of volume change at HTM population scale, obtained in Fig. 10, are plotted in Fig. 13 as coloured triangles for each volume fraction. They are compared with the results obtained on a custom test bench, in which hydrostatic compression is also performed, but using a different imaging technique [31]. In this test, digital image correlation provides the macroscopic response of the (matrix + HTM) composite. The longitudinal ε_{xx} and transverse ε_{yy} small strain tensor components are measured on the end-surface of a composite sample (2D measurements). The corresponding change in volume is then estimated from the trace of strain tensor (see [31] for technical details)

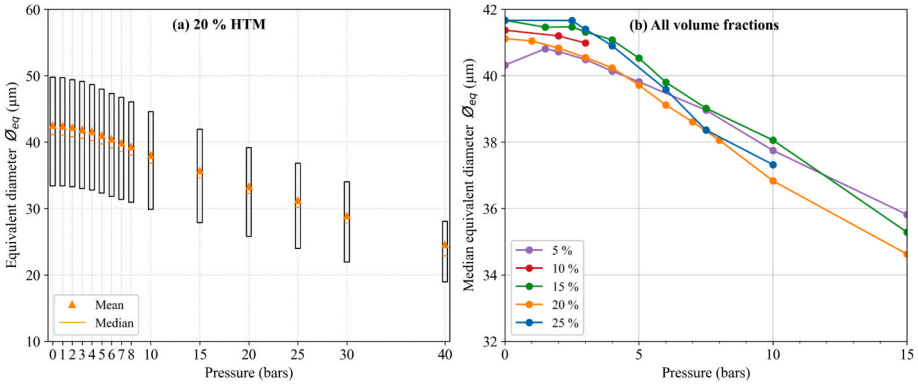

Fig. 9. (a) Descriptive statistics of equivalent diameter during pressure ramp for the 20 % HTM material. (b) Median equivalent diameter change as a function of pressure, for all volume fractions.

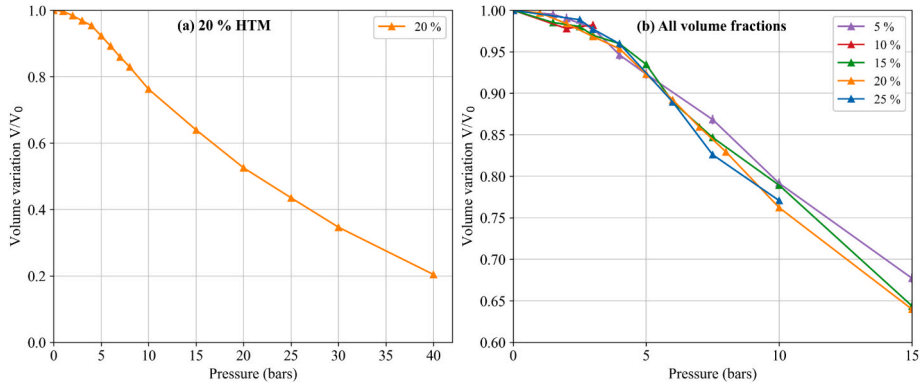

Fig. 10. HTM total volume change during pressure ramp for (a) the 20 % HTM material, and (b) all volume fractions.

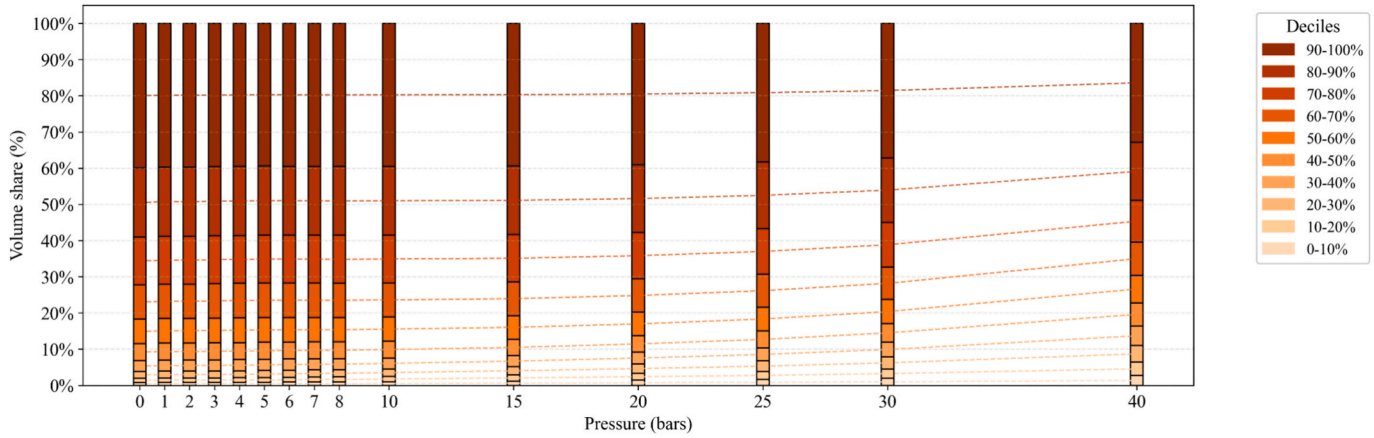

Fig. 11. Deciles volume share in the total HTM volume, as a function of pressure, for the 20 % HTM material. Dashed lines are guides for the eyes.

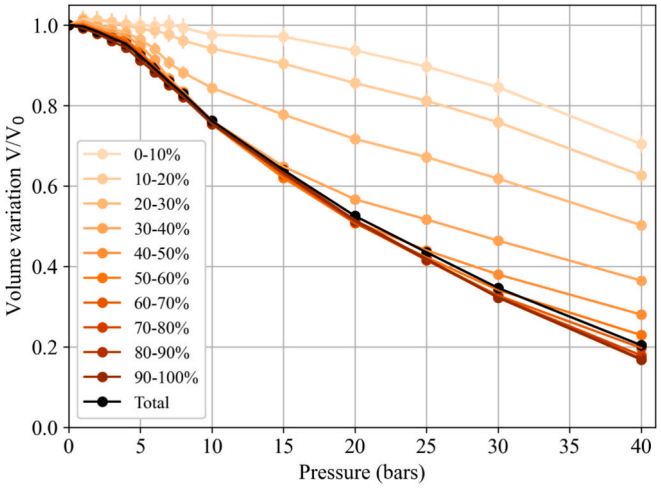

Fig. 12. Volume change of each decile during pressure ramp, confronted with total HTM volume change, for the 20 % HTM material.

$$\frac{\widetilde{V}}{\widetilde{V}_0} = 1 + \frac{3(\varepsilon_{xx} + \varepsilon_{yy})}{2}. \tag{7}$$

However, in this case, the composite volume change cannot be directly compared with that obtained from the tomography. Indeed, the left-hand side ratio in Eq. (7) encompasses the volumes of both the matrix and the microspheres. To isolate the contribution of the microspheres, we assume an incompressible matrix, thereby attributing the entire volume change to the one of the microspheres. Under this assumption, the normalized volume change δ is

$$\delta = 1 + \frac{3(\varepsilon_{xx} + \varepsilon_{yy})}{2f_v}, \tag{8}$$

where the volume fraction f_v has already been given in Table 2. Data associated with each f_v is shown as curves in Fig. 13, where δ can be compared with the volume change of the microspheres obtained in tomography. Despite some deviations, both types of tests reveal similar trends, with a decrease in the ratio, along with an intensification occurring before reaching 5 bars. The normalized volume change measured on the composite therefore closely follows that of the microspheres for all investigated volume fractions, suggesting that, within this pressure range, attributing the deformation solely to the microspheres is a relevant assumption.

3.3. *Returning back to ambient pressure*

Quantitative volume measurements of the microspheres before and after the pressure cycle are provided in Table 4. Volume changes remain below –5% for individual spheres and decrease to –2.3 % when considering the entire population, indicating limited overall variation. It is highly likely that these differences decline further if the material relaxes at ambient pressure before measurement (which was not the case here). This is consistent with the visual examination presented in Appendix 3, that does not reveal any notable difference in microspheres shape before and after pressurization. Nevertheless, it must be acknowledged that the present analysis focuses on the remanent volume change of the microspheres only, without accounting for the

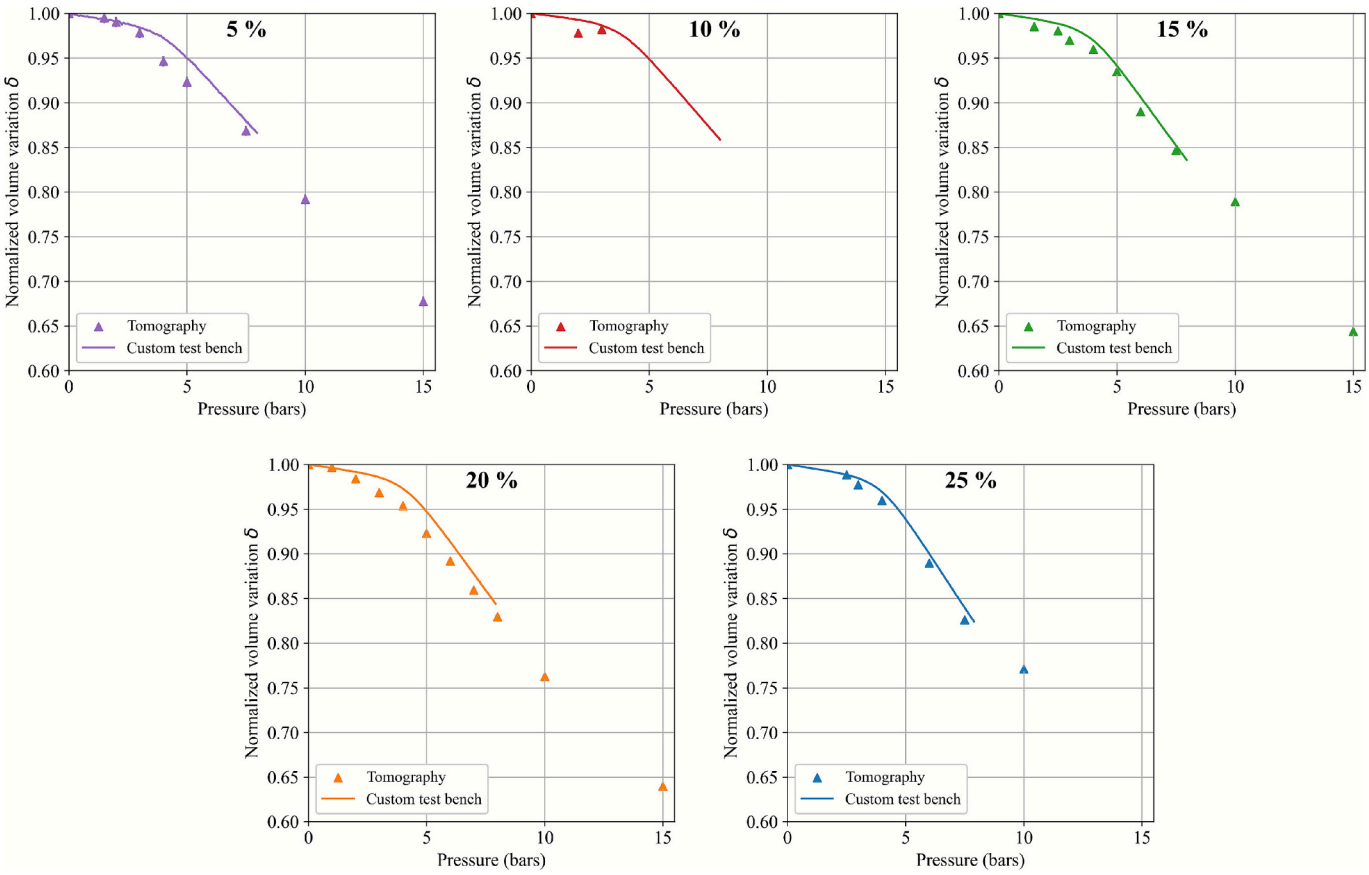

Fig. 13. Volume change during pressure ramp for all volume fractions, by means of two independent experimental protocols.

Table 4
Microspheres change in volume after the pressure cycle.

Microsphere	a	b	c	d	Population
Change in volume	− 1.3 %	− 4.3 %	+ 0.4 %	− 2.3 %	− 2.3 %

microsphere–matrix interface. Investigating the potential interfacial damage under repeated pressure cycles will be the subject of future work.

These results demonstrate an exceptional reversibility in the response of HTM, which are able to recover their entire volume without damage, despite the severe post-buckling observed in Fig. 6 and Fig. 7. It aligns with the high elastic recovery already evidenced for similar materials [30,50].

4. Preliminary modelling investigations

While several models have been proposed in the literature, only a few have been compared with experimental data, especially at the microspheres scale. In the following, we propose some insights for the mechanical modelling of the Buckle Gum.

As shown above, the volume change of the thermoplastic spheres is in agreement with the response of the composite during the pressure ramp. During this loading sequence, microspheres experience three successive deformation regimes: pre-buckling, buckling and post-buckling. While the change in volume could, in principle, be modelled independently within each regime, combining these contributions into a unified model for a polydisperse composite remains a considerable challenge. In the following, preliminary modelling developments for pre- and post-buckling regimes are proposed separately.

As illustrated in Fig. 14, the Buckle Gum can be considered as a

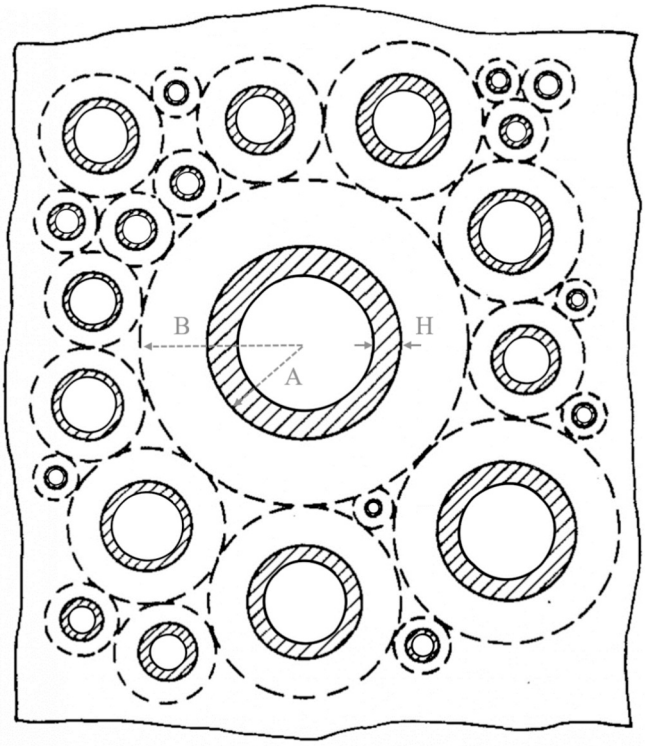

Fig. 14. Hashin's "Composite Sphere Assemblage" [51], adapted for hollow inclusions.

distribution of *"Composite Spheres (CS)"* made of hollow thermoplastic shells of thickness H (dashed) embedded in elastomer spheres (plain white) of internal and external radii A and B, such that

$$A/B = f_v^{1/3}. \tag{9}$$

This construction, referred to as the *"Composite Sphere Assemblage (CSA)"*, was first introduced by Hashin for linear elastic matrices and inclusions [51]. In this model, all microspheres admit the same wall thickness ratio:

$$X = H/A \tag{10}$$

4.1. Pre-buckling regime: A linear elastic composite

First, the focus is laid on the pre-buckling regime. Specifically, we aim to evaluate whether the averaged shell properties optimized from macroscopic hydrostatic measurements are in agreement with the material microstructure. If so, an equivalent monodisperse material can be defined to effectively represent the pre-buckling behaviour, providing a practical framework for design and prediction.

4.1.1. Bulk modulus

Case of thick spherical spheres: .H = A

In the particular case of solid inclusions, Hashin's theory provides an exact analytical expression for the effective bulk modulus K^*:

$$K^* = K_m + (K_s - K_m)\frac{f_v(3K_m + 4G_m)}{3[f_v K_m + (1 - f_v)K_s] + 4G_m}, \tag{11}$$

where K_m and K_s are the bulk moduli of the matrix and solid spheres, respectively, and G_m is the matrix shear modulus. This expression is independent of the microsphere size distribution.

Case of hollow spherical shells:.H < A

The case of hollow inclusions, illustrated in Fig. 14, was later formulated by Lee and Westmann [52] as a straightforward extension of Hashin's work, and reworked ever since [53]. The effective bulk modulus K^* is then expressed as

$$K^* = K_m\frac{\delta_{ms}(1 + f_v\gamma_m) + k_s\gamma_m(1 - f_v)}{\delta_{ms}(1 - f_v) + k_s(\gamma_m + f_v)}, \tag{12}$$

with

$$\gamma_m = \frac{4G_m}{3K_m};\ k_s = \frac{4G_s}{3K_s} + (1 - X)^3;\ \ \delta_{ms} = \frac{4G_s}{3K_m}\left[1 - (1 - X)^3\right], \tag{13}$$

where G_s is the shear modulus of the microspheres material.

Case of hollow spherical shells: H < A with incompressible matrix.

When the matrix is assumed incompressible, $(K_m \to +\infty)$, Eq. (12) simplifies to

$$K^* = \frac{\frac{4G_s}{3}\left[1 - (1 - X)^3\right] + \frac{4G_m}{3}\left[\frac{4G_s}{3K_s} + (1 - X)^3\right](1 - f_v)}{\left[\frac{4G_s}{3K_s} + (1 - X)^3\right]f_v}. \tag{14}$$

Finally, in the pre-buckling regime, the volume change of the composite can be calculated as

$$\frac{\widetilde{V}}{\widetilde{V}_0} = 1 - \frac{p}{K^*}, \tag{15}$$

where p is the applied pressure and K^* is given by Eq. (14).

In the following, the effective bulk modulus K^* of Eq. (14) is used to determine optimized shell properties under the assumption of an equivalent monodisperse distribution of microspheres.

4.1.2. Estimated homogenized shell properties

The applicability of Eq. (14) must first be carefully inspected. As noted earlier, it is strictly valid only for a constant X, i.e. when shells thickness H scales proportionally with the internal radius A. However, as shown in [41] and discussed in Section 3.2.1, H exhibits little dependence on the particle size in the Buckle Gum. This implies that the model is effectively valid only for a fixed microsphere radius A, corresponding to a monodisperse approximation of the actual microsphere radius distribution.

Within this framework, homogenized shell properties can be estimated in two ways: either by fixing the shell thickness from Curd et al. [41] and adjusting the particle radius to match the bulk modulus from mechanical tests, or by using the particle radius from our tomography data and adjusting the shell thickness accordingly. Motivated by the work of Yousaf et al. for uniaxial tension and the Generalized Self-Consistent Method (GSCM, [38,41]), we adopt here the second approach, which leverages measured particle sizes and calibrates the shell thickness to reproduce the macroscopic bulk response.

Fig. 15 illustrates the determination of the homogenized shell thickness by plotting the bulk modulus K^* as a function of the equivalent microsphere diameter $\varnothing_{eq}$. K^* values decrease with increasing volume fraction, reflecting that the combination of elastomer matrix and microspheres moves the response away from a purely incompressible matrix. This trend is observed for both the experimental and the modelled values. Particular attention should be paid to the intersections between experimental and estimated K^* curves: for a given volume fraction, this intersection reveals the (A, H) pairs for which the model reproduces the experimental results. In other words, it defines the shell properties for which the monodisperse model is mechanically equivalent to the real polydisperse composite. Remarkably, the intersections always fall within the light-shaded envelope, i.e., within one standard deviation around the median equivalent diameter $\overline{\varnothing_{eq}}$. As the shell thickness H varies, the intersect shifts, and for a moderate decrease of H, it approaches $\overline{\varnothing_{eq}}$. This allows the determination of an optimal shell thickness H_{opt}, for which the experimental and estimated K^* values match exactly at $\overline{\varnothing_{eq}}$. The corresponding values of K^*, $\overline{\varnothing_{eq}}$ and H_{opt} are reported in Table 5.

The optimized shell thickness is revealed independent of the microsphere volume fraction and ranges from 0.22 to 0.24 μm. This observation is consistent with expectations, since the shell thickness should primarily depend on the manufacturing process rather than the microsphere concentration. When compared to the experimental measurements of Curd et al. (Fig. 5 in [41]), our estimated values lie in the standard deviation, although slightly lower. In contrast, they are in striking agreement with the optimized shell thicknesses identified in uniaxial tension by Yousaf et al. [38].

Thus, the present Composite Sphere Assemblage monodisperse model calibrated against our macroscopic experiments provides a realistic representation of the actual microsphere geometry and effectively captures the material response in the pre-buckling regime.

4.2. Post-buckling regime: A hyperelastic material with pores

As the applied pressure increases, each microsphere eventually reaches its critical buckling pressure p_c. Similarly than in the model proposed by De Pascalis et al. [35], it is considered that beyond this pressure the microsphere has no more stiffness. Thus, the Composite Spheres Assemblage of Fig. 14 reduces to elastomer spheres surrounding pores. Following Hashin's approach applied to large strain elastic material [54], after buckling of all microspheres the material behaviour is driven by the mechanical response of a *thick spherical shell*, of outer radius B and inner radius $A = B \times f_v^{1/3}$ (Eq. (9)), subjected to external hydrostatic pressure.

To derive this response, let first define the stretch ratios λ_a and λ_b at inner and outer radii, respectively,

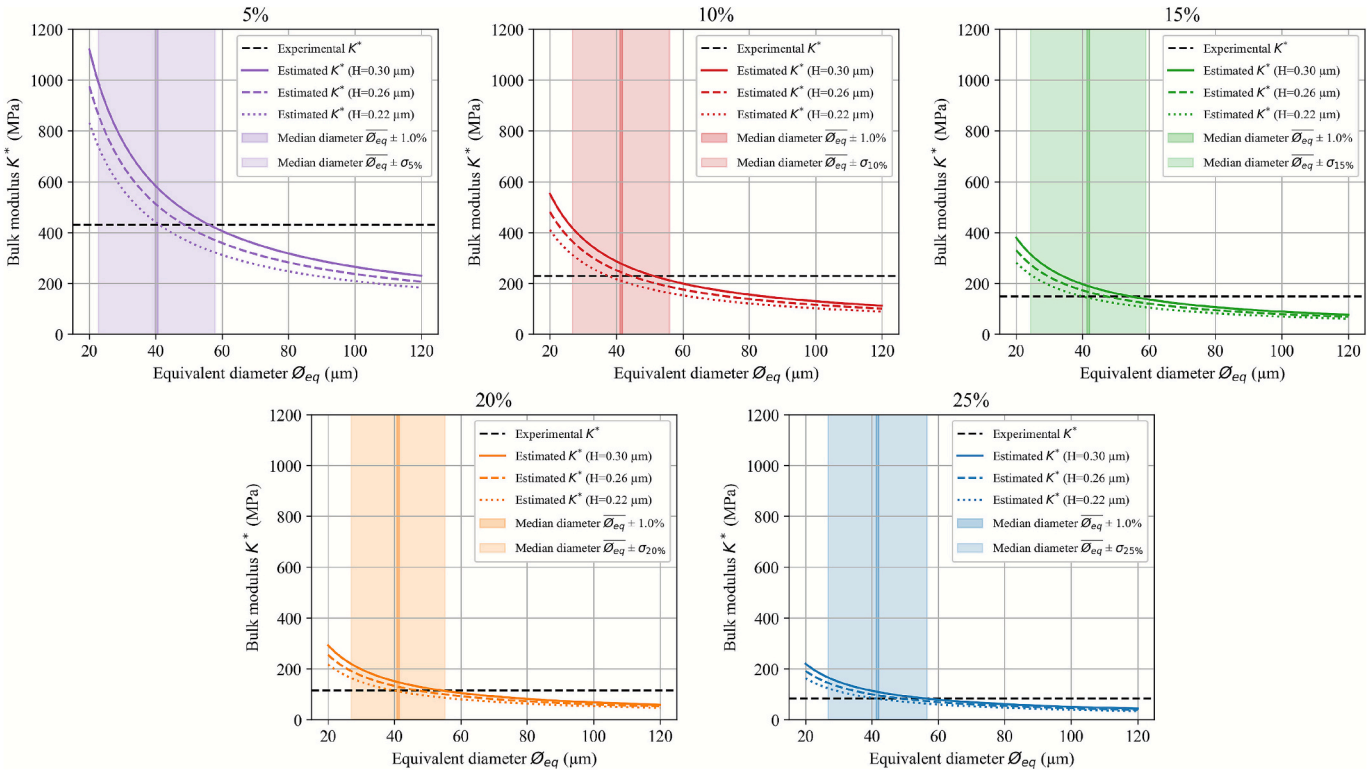

Fig. 15. Bulk modulus as function of equivalent diameter for all volume fractions. For each volume fraction, a light-shaded envelope representing standard deviation σ_{V_f} is drawn around the median diameter $\overline{\varnothing_{eq}}$ determined from Fig. 4b. A darker, narrower, envelope encompasses a ± 1 % variation around this median value. Black horizontal dashed lines correspond to the experimental values of K^* obtained from macroscopic hydrostatic tests on the composite materials, while the coloured curves represent the estimated K^* values calculated from Eq. (14), with different linestyles corresponding to the tested thicknesses H.

Table 5
Optimized monodisperse shell properties matching experimental bulk modulus.

Specified volume fraction (%)	Bulk modulus K^* (MPa)	Median equivalent diameter $\overline{\varnothing_{eq}}$ (μm)	Optimized thickness H_{opt} (μm)
5	429.9	40.3	0.22
10	229.2	41.4	0.24
15	148.2	41.7	0.23
20	113.9	41.1	0.23
25	82.7	41.7	0.22

$$\lambda_a = \frac{a}{A}, \quad \lambda_b = \frac{b}{B}, \tag{16}$$

where a and b are the deformed inner and outer radii, respectively. Assuming incompressibility, stretch ratios are related by

$$\lambda_a = \left(\frac{\lambda_b{}^3 - 1}{f_v} + 1\right)^{1/3}, \tag{17}$$

where f_v now corresponds to the volume fraction of porosities. For the solution to remain physically admissible, λ_a should remain positive.

According to De Botton et al. [55], the relationship between the hydrostatic pressure above critical pressure, $\Delta p = p - p_c$, applied on the elastomer sphere outer radius B and its deformation can be written as

$$\Delta p = \int_{\lambda_a}^{\lambda_b} \frac{dW}{d\lambda} \frac{1}{\lambda^3 - 1} d\lambda, \tag{18}$$

where λ is the circumferential stretch ratio in the elastomeric sphere, and W is the strain energy density of the elastomer matrix expressed in the special case of hydrostatic deformation. Here, the strain of the elastomer matrix being moderate, the neo-Hookean model is adopted for W. The shear modulus being denoted μ, the complete complete derivation of Eq. (18), detailed in Appendix 4, yields to

$$\Delta p = 2\mu \left[\frac{1}{\lambda_a} + \frac{1}{4\lambda_a{}^4} - \left(\frac{1}{\lambda_b} + \frac{1}{4\lambda_b{}^4}\right)\right]. \tag{19}$$

As emphasized above, Eq. (19) is only valid above the critical pressure p_c. This implies that, in theory, this equation is valid from the deformed Composite Sphere Assemblage at the very end of the pre-buckling stage. In fact, determining this exact configuration is difficult because of the progressive buckling of the microspheres. In order to investigate the relevance of this post-buckling model, we adopt the hypothesis that the deformation due to pre-buckling is small enough not to be taken into account, thus that the "buckled state" has λ_a and λ_b so close to unity that it can be considered equal to the "initial state", for which $\delta = 1$. Note that this assumption is mandatory to directly apply the Composite Sphere Assemblage theory proposed in [54]. By doing so, the normalized change in volume reduces to

$$\delta = \lambda_a{}^3. \tag{20}$$

It is the change in volume of the inner elastomer radius, in other words the cavity with the buckled microsphere. By solving numerically Eq. (19), δ is calculated as a function of the change in pressure Δp. To determine the absolute pressure p, the curves δ vs. Δp must be shifted by the critical pressure. For this purpose, we rely on the work of [31], who identified the onset of buckling by detecting the maximum slope variation of the continuous experimental curves. They report a critical pressure of approximately 4.0 bars for all volume fractions (see their Table 3), which remarkably coincides with our critical pressure calculated for the largest spheres in Section 3.2.1. These values are used to horizontally shift the post-buckling curves so that the intersection with the pre-buckling regime occurs at 4 bars.

With this pressure shift, the model approaches the experimental

curve at the onset of the post-buckling regime. However, as the pressure increases, the deviation between the model and the experimental data becomes more pronounced. In fact, this discrepancy arises because the model is a clear simplification of the post-buckling response. Especially, loss of spherical symmetry and influence of the pre-buckling regime were neglected, which are admittedly strong assumptions deserving deeper analysis.

4.3. The challenge of post-buckling onset

As shown in Fig. 16, if the pre-buckling satisfactorily reproduces the experimental curve, the post-buckling model fails to capture both the onset of this phenomenon and the corresponding critical pressure. Moreover, the compatibility of the predictions for both regimes should be discussed.

The pre-buckling model is based on a mechanically equivalent monodisperse material, for which buckling theoretically occurs at a single critical well-defined pressure, resulting in an abrupt slope change in the response curve. This is not what is experimentally observed: in reality the microspheres buckle progressively depending on their size ratio X , as shown in Fig. 8. As a consequence, the actual transition between pre- and post-buckling regimes is smooth, with a gradual change in curvature of the pressure–volume curves. This effect is induced by the microsphere distribution polydispersity, which renders difficult the definition of a precise critical pressure. In addition, the tomography resolution does not allow for a precise identification of this threshold neither, making it challenging to consistently unify the predictions of pre- and post-buckling in the neighbourhood of the critical pressure.

Finally, accurately capturing the progressive contribution of buckled microspheres, and integrating this progressive response with respect to their size remains a challenging task that will be addressed in future work.

5. Conclusions

In this article, the behaviour of the *Buckle Gum*, an elastomer matrix composite filled with hollow thermoplastic microspheres, was investigated: we observed the mechanical response of this material under hydrostatic compression thanks to an experimental set-up embedded in a tomograph.

Owing to tomographic resolution, the observations were limited to the post-buckling regime, where *in situ* imaging revealed the deformation of HTM under increasing pressure. This regime occurs after reaching a critical pressure depending on the geometry of the considered microsphere. It causes a gradual shrinkage of the particle and deviation from perfect sphericity. The buckling of an increasing number of microspheres lead to volume change of the whole population. Among its constituents, the largest microspheres are responsible for the majority of the population volume, and thus dictate the overall behaviour. These tomography findings are consistent independently of the HTM volume fraction at least up to 10 bars, and are corroborated by macroscopic mechanical experiments on the composite material. HTMs exhibit a remarkable recoverability of their initial volume after a pressure cycle. Contrary to hollow glass microspheres, no persistent damage is reported for HTM when returned to ambient pressure, although potential interfacial debonding should be further investigated.

The exceptional properties of the *Buckle Gum* hold significant potential for pressure-related applications. Whereas previous models have rarely been confronted with experimental data, our inverse modelling approach has been applied to Composite Spheres Assemblage models for both pre- and post-buckling regimes. It satisfactorily approximates the material response across all volume fractions for both regimes, but fail to predict the critical pressure. Future work will aim to unify these formulations and address the remaining challenges associated with microsphere polydispersity.

CRediT authorship contribution statement

H. Madeira: Writing – review & editing, Writing – original draft, Visualization, Methodology, Formal analysis, Data curation, Conceptualization. **L. Tanné:** Writing – review & editing, Methodology, Investigation, Formal analysis, Conceptualization. **I. Pivdiablyk:** Writing – review & editing, Methodology, Conceptualization. **M. Coret:** Writing –

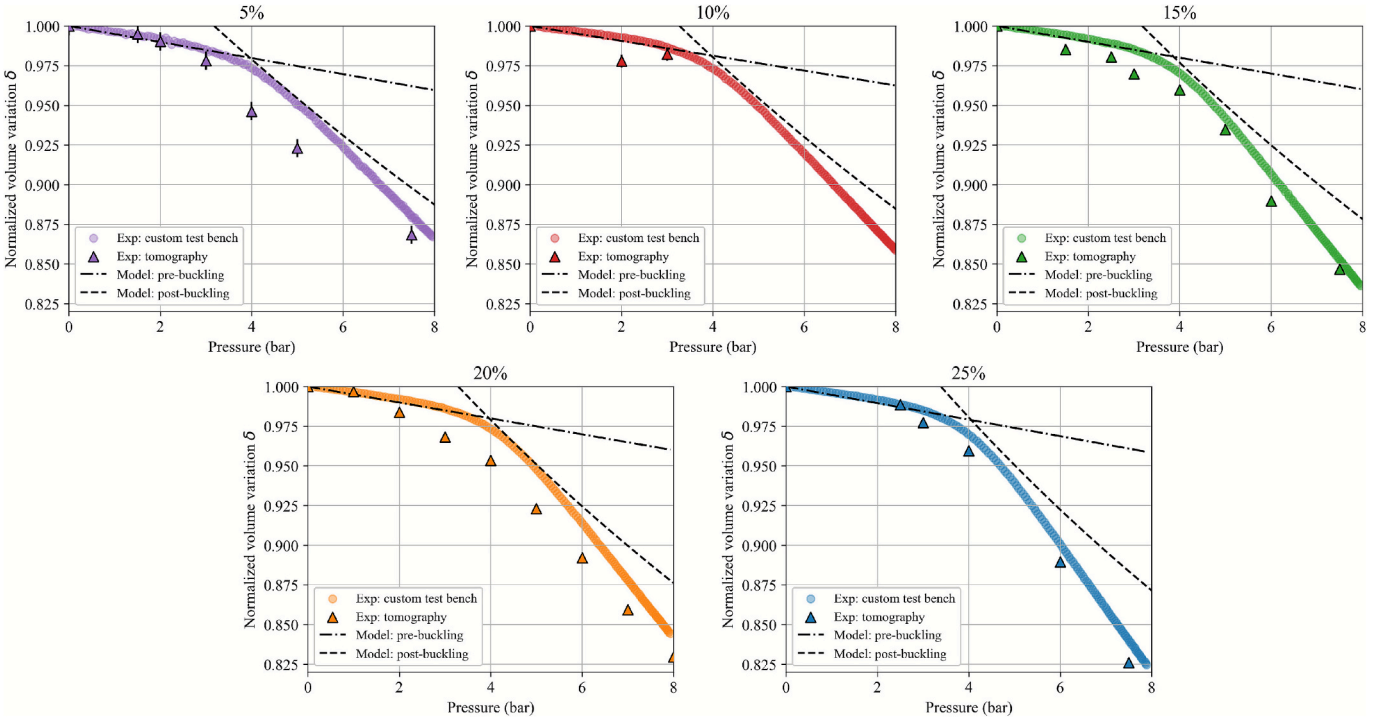

Fig. 16. Pre- and post-buckling models compared to experimental data, for all volume fractions.

review & editing, Supervision, Methodology, Funding acquisition, Conceptualization. **P. Rublon:** Writing – review & editing, Resources, Methodology, Funding acquisition, Conceptualization. **J. Papillon:** Writing – review & editing, Resources, Investigation. **J. Adrien:** Writing – review & editing, Resources, Investigation. **E. Verron:** Writing – review & editing, Supervision, Project administration, Methodology, Funding acquisition, Conceptualization.

Declaration of competing interest

The authors declare that they have no known competing financial interests or personal relationships that could have appeared to influence the work reported in this paper.

Acknowledgements

The authors thank Gaëlle Daoudal for her help with the experiments. This work was carried out within a research collaboration driven by Centrale Nantes, with funding provided by the French Agence Nationale de la Recherche (ANR), Naval Group, and CETIM as part of project ANR-24-CHIN-0006-01.

Appendix 1:. Image analysis post-processing

Raw images at a given pressure level reconstruct a $1200 \times 1200 \times 1200\ \mu m^3$ volume. They are post-processed to separate the HTM from the matrix and from each other. These operations, performed with Fiji [56], follow the flowchart presented in Fig. A1.

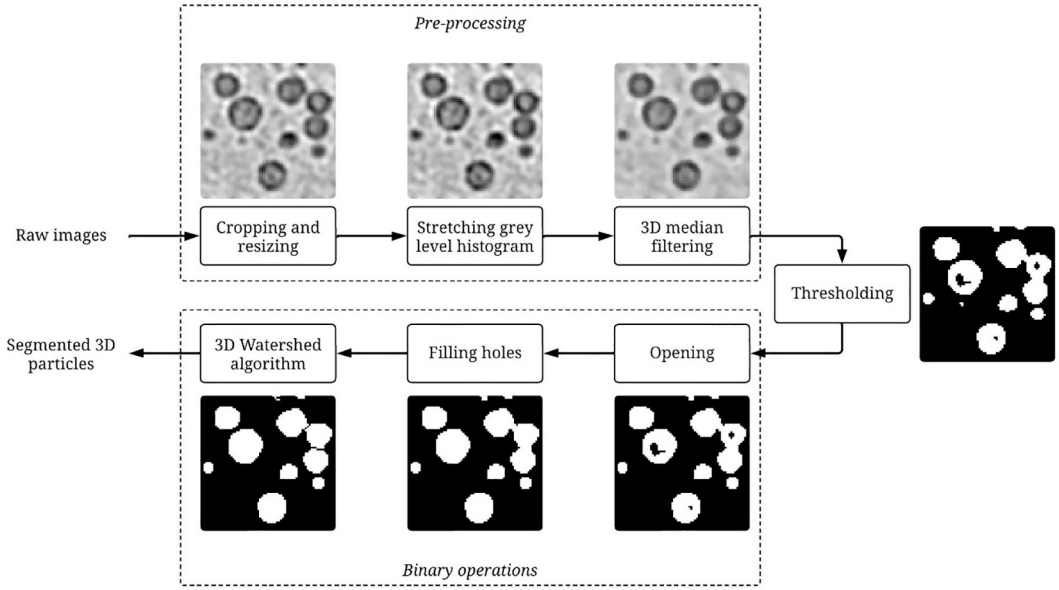

Fig. A1. Post-processing operations performed on tomographic images.

First, several pre-processing operations are performed to prepare the images thresholding. The volume is cropped to $500 \times 500 \times 500\ \mu m^3$ to eliminate boundary effects, without affecting statistical representativeness. The grey histogram is stretched to enhance contrast, then a 3D median filter is applied to reduce noise, while conserving HTM edges. By the end of the pre-processing, thresholding is performed to convert greyscale images to binary ones. Second, binary operations are performed to refine the segmentation, starting with an opening and the filling holes operation. Finally, particles are separated from each other using MorphoLibJ's 3D watershed algorithm with a city-block distance map [57]. Each HTM is labelled and its useful geometric properties are determined, namely the particle volume V, as well as the smallest encompassing ellipsoid volume $\widehat{V}$ and surface area $\widehat{S}$, calculated by Crofton's method.

Appendix 2:. Pressure impact on sphericity at HTM population scale

Deviation from perfect sphericity is quantified using Wadell sphericity ψ calculated from the smallest encompassing ellipsoid volume $\widehat{V}$ and surface area $\widehat{S}$ of each individual microsphere:

$$\psi = \frac{\pi^{1/3}\left(6\times\widehat{V}\right)^{2/3}}{\widehat{S}}. \quad \text{(A2-1)}.$$

The change in sphericity is plotted in Fig. A2a for the 20 % HTM material during the pressure ramp. A ψ plateau is observed, with an evolution that only seems to start from 15-20 bar, while remaining on high sphericity values. This seems fairly consistent with what can be observed qualitatively on Fig. 7, with particles starting to move away from perfect sphericity at similar pressures while remaining relatively spherical. Furthermore, the mean value appears to be distant from the other statistical indicators: this effect is likely due to the smallest microspheres (below first quartile), whose poor voxel resolution artificially lowers the mean. As shown in Fig. A2b, the values of ψ are similar whatever the volume fraction considered. As the experiments did not exceed 15 bars for the other formulations, it is difficult to discuss the independence of the sphericity drop towards volume fraction.

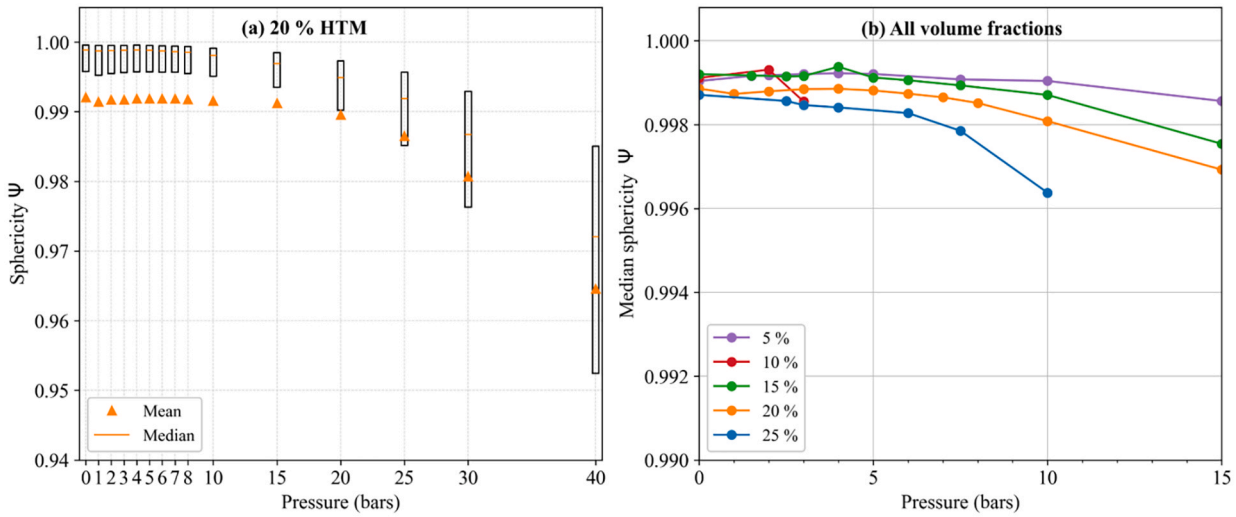

Fig. A2. (a) Descriptive statistics of sphericity during pressure ramp for the 20 % HTM material. (b) Median sphericity changes as a function of pressure, for all volume fractions.

Appendix 3:. Visualization of microspheres before and after pressure cycle

Fig. A3 shows the four microspheres already presented in Fig. 5, before and after the pressure cycle. Visual examination does not reveal any notable difference: the microspheres recover their initial shape.

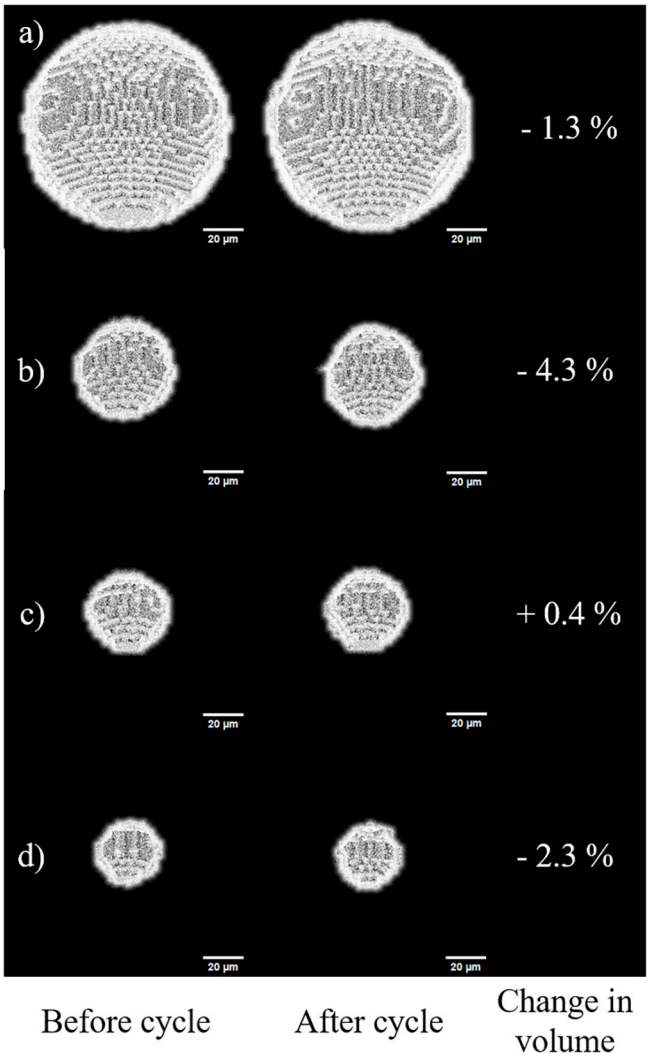

Fig. A3. Individuals from the (a) 90-100 %, (b) 70-80 %, (c) 50-60 % and (d) 20-30 % deciles of the 20 % HTM material, before and after a pressure cycle.

Appendix 4:. Derivation of eq. (18)

The Neo-Hookean strain energy density in the special case of hydrostatic deformation writes

$$W = \frac{\mu}{2}\left(2\lambda^2 + \frac{1}{\lambda^4} - 3\right), \tag{A4-1}$$

with μ the shear modulus of the material and λ is the circumferential stretch ratio. Hence,

$$\frac{dW}{d\lambda} = 2\mu\left(\lambda - \frac{1}{\lambda^5}\right), \tag{A4-2}$$

and partial fraction decomposition of Eq. (18) yields

$$\Delta p = \int_{\lambda_a}^{\lambda_b} 2\mu \frac{\lambda^6 - 1}{\lambda^5\left(\lambda^3 - 1\right)}\, d\lambda\,. \tag{A4-3}$$

Integration of Eq. (A4-3) leads to Eq. (19).

Appendix 5. Supplementary data

Supplementary data to this article can be found online at https://doi.org/10.1016/j.matdes.2025.115234.

Data availability

Because of the sensitive nature of the industrial application, authors do not have permission to share raw data. However, codes and image analysis macros will be made available on demand.

References

[1] M. Tomalino, G. Bianchini, Heat-expandable microspheres for car protection production, Prog. Org. Coat. 32 (1–4) (1997) 17–24, https://doi.org/10.1016/S0300-9440(97)00080-5.

[2] B. Zeqiri, C.J. Bickley, A new anechoic material for medical ultrasonic applications, Ultrasound Med. Biol. 26 (3) (2000) 481–485, https://doi.org/10.1016/S0301-5629(99)00147-7.

[3] H. Im, S.C. Roh, C.K. Kim, Fabrication of Novel polyurethane Elastomer Composites Containing Hollow Glass Microspheres and their Underwater applications, Ind. Eng. Chem. Res. 50 (12) (2011) 7305–7312, https://doi.org/10.1021/ie102600q.

[4] N. Gupta, S.E. Zeltmann, V.C. Shunmugasamy, D. Pinisetty, Applications of Polymer Matrix Syntactic Foams, JOM 66 (2) (2014) 245–254, https://doi.org/10.1007/s11837-013-0796-8.

[5] X. Huang, J. Gao, W. Li, H. Xue, R.K.Y. Li, Y.-W. Mai, Preparation of poly (ε-caprolactone) microspheres and fibers with controllable surface morphology, Mater. Des. 117 (2017) 298–304, https://doi.org/10.1016/j.matdes.2016.12.096.

[6] J. Park, S.H. Yang, K.S. Minn, C.B. Yu, S.Y. Pak, Y.S. Song, J.R. Youn, Design and numerical analysis of syntactic hybrid foam for superior sound absorption, Mater. Des. 142 (2018) 212–220, https://doi.org/10.1016/j.matdes.2018.01.040.

[7] F.A. Shutov, 'Syntactic polymer foams', in *Chromatography/Foams/Copolymers*, in advances in Polymer Science **73/74**, Springer, Berlin Heidelberg 63–123 (1986), https://doi.org/10.1007/3-540-15786-7_7.

[8] V.V. Budov, Hollow glass microspheres. use, properties, and technology (Review), Glass Ceram. 51 (7–8) (1994) 230–235, https://doi.org/10.1007/BF00680655.

[9] D. Choqueuse, Etude expérimentale et analyse du comportement de mousses syntactiques pour grande profondeur d'immersion, Université de Bretagne Occidentale, 2012. PhD Thesis.

[10] D. Carolan, A. Mayall, J.P. Dear, A.D. Fergusson, Micromechanical modelling of syntactic foam, Compos. Part B Eng. 183 (2020) 107701, https://doi.org/10.1016/j.compositesb.2019.107701.

[11] M. Le Gall, D. Choqueuse, P.-Y. Le Gac, P. Davies, D. Perreux, Novel mechanical characterization method for deep sea buoyancy material under hydrostatic pressure, Polym. Test. 39 (2014) 36–44, https://doi.org/10.1016/j.polymertesting.2014.07.009.

[12] Loubrieu, Durability of Syntactic Foams in Deep Sea Environment, Université de Bretagne Occidentale, 2022. PhD Thesis.

[13] J. Wang, B. Gao, W. Cui, A method for improving the hydrostatic pressure testing of the compressive strength of solid buoyancy materials used at full ocean depth, Ocean Eng. 286 (2) (2023) 115673, https://doi.org/10.1016/j.oceaneng.2023.

[14] J.A. Brown, J.D. Carroll, B. Huddleston, Z. Casias, K.N. Long, A multiscale study of damage in elastomeric syntactic foams, J. Mater. Sci. 53 (14) (2018) 10479–10498, https://doi.org/10.1007/s10853-018-2263-y.

[15] L. Bardella, F. Malanca, P. Ponzo, A. Panteghini, M. Porfiri, A micromechanical model for quasi-brittle compressive failure of glass-microballoons/thermoset-matrix syntactic foams, J. Eur. Ceram. Soc. 34 (11) (2014) 2605–2616, https://doi.org/10.1016/j.jeurceramsoc.2013.11.045.

[16] A. Panteghini, L. Bardella, On the compressive strength of glass microballoons-based syntactic foams, Mech. Mater. 82 (2015) 63–77, https://doi.org/10.1016/j.mechmat.2014.12.005.

[17] J. Adrien, E. Maire, N. Gimenez, V. Sauvantmoynot, Experimental study of the compression behaviour of syntactic foams by in situ X-ray tomography, Acta Mater. 55 (5) (2007) 1667–1679, https://doi.org/10.1016/j.actamat.2006.10.027.

[18] J. Lachambre, E. Maire, J. Adrien, D. Choqueuse, In situ observation of syntactic foams under hydrostatic pressure using X-ray tomography, Acta Mater. 61 (11) (2013) 4035–4043, https://doi.org/10.1016/j.actamat.2013.03.017.

[19] M.E. Kartal, L.H. Dugdale, J.J. Harrigan, M.A. Siddiq, D. Pokrajac, D.M. Mulvihill, Three-dimensional in situ observations of compressive damage mechanisms in syntactic foam using X-ray microcomputed tomography, J. Mater. Sci. 52 (17) (2017) 10186–10197, https://doi.org/10.1007/s10853-017-1177-4.

[20] X. Zhang, P. Wang, Y. Zhou, X. Li, E.-H. Yang, T.X. Yu, J. Yang, The effect of strain rate and filler volume fraction on the mechanical properties of hollow glass microsphere modified polymer, Compos. Part B Eng. 101 (2016) 53–63, https://doi.org/10.1016/j.compositesb.2016.06.079.

[21] G. Zhai, Y. Ding, Z. Ma, Z. Wei, X. Li, B. Liu, Novel triaxial experimental investigation on compressive behavior of hollow glass microspheres composites under varied temperature environments, Polym. Test. 115 (2022) 107745, https://doi.org/10.1016/j.polymertesting.2022.107745.

[22] Nouryon, 'Technical Data Sheet Expancel® DE Microspheres', 2024.

[23] R. Shorter, The mechanical behaviour of elastomers when hollow microspheres are used as a particulate filler, Queen Mary University of London, School of Engineering and Material Science, 2014. PhD Thesis.

[24] W.T. Van Der Heijden, M.A. Arnold, Koiter's Elastic Stability of Solids and Structures, Cambridge University Press (2008), https://doi.org/10.1017/CBO9780511546174.

[25] J.W. Hutchinson, Buckling of spherical shells revisited, Proc. R. Soc. Math. Phys. Eng. Sci. 472 (2195) (2016) 20160577, https://doi.org/10.1098/rspa.2016.0577.

[26] D.P. Holmes, J.-H. Lee, H.S. Park, M. Pezzulla, Nonlinear buckling behavior of a complete spherical shell under uniform external pressure and homogenous natural curvature, Phys. Rev. E 102 (2) (2020) 023003, https://doi.org/10.1103/PhysRevE.102.023003.

[27] M. Bour, Caractérisation et modélisation du comportement mécanique d'élastomères compressibles, Université de Tours, 2023. PhD Thesis.

[28] M. Coret, E. Verron, P. Rublon, B. Leblé, Remarkable response of hollow thermoplastic microspheres-elastomer matrix composites in uniaxial tension, Mech. Soft Mater. 4 (1) (2022) 8, https://doi.org/10.1007/s42558-022-00046-1.

[29] K.R. Dando, W.M. Cross, M.J. Robinson, D.R. Salem, Production and characterization of epoxy syntactic foams highly loaded with thermoplastic microballoons, J. Cell. Plast. 54 (3) (2018) 499–514, https://doi.org/10.1177/0021955X17700093.

[30] Z. Yousaf, M. Smith, P. Potluri, W. Parnell, Compression properties of polymeric syntactic foam composites under cyclic loading, Compos. Part B Eng. 186 (2020) 107764, https://doi.org/10.1016/j.compositesb.2020.107764.

[31] B. Ruelle, P. Rublon, M. Coret, and E. Verron, 'Compressibility of elastomer matrix-hollow thermoplastic microspheres composites under low hydrostatic pressure', Strain **61**(4), 2025, doi: 10.1111/str.70013.
[32] K.M. Moerman, B. Fereidoonnezhad, J.P. McGarry, Novel hyperelastic models for large volumetric deformations, Int. J. Solids Struct. 193–194 (2020) 474–491, https://doi.org/10.1016/j.ijsolstr.2020.01.019.
[33] M. Bour, S. Méo, G. Le Quilliec, F. Chalon, M. Raymond, D. Picart, Phenomenological constitutive laws for the dissipative behaviour of highly compressible elastomers and their finite element implementation, Eur. J. Mech. - ASolids 109 (2025) 105442, https://doi.org/10.1016/j.euromechsol.2024.105442.
[34] S.-L. Fok, D.J. Allwright, Buckling of a spherical shell embedded in an elastic medium loaded by a far-field hydrostatic pressure, J. Strain Anal. Eng. Des. 36 (6) (2001) 535–544, https://doi.org/10.1243/0309324011514692.
[35] R. De Pascalis, I. David Abrahams, W.J. Parnell, Predicting the pressure–volume curve of an elastic microsphere composite, J. Mech. Phys. Solids 61 (4) (2013) 1106–1123, https://doi.org/10.1016/j.jmps.2012.11.005.
[36] G.W. Jones, M.J.A. Smith, M. Thorpe, I.D. Abrahams, W.J. Parnell, Transition from equatorial to whole-shell buckling in embedded spherical shells under axisymmetric far-field loading, Int. J. Solids Struct. 256 (2022) 111957, https://doi.org/10.1016/j.ijsolstr.2022.111957.
[37] R.M. Christensen, K.H. Lo, Solutions for effective shear properties in three phase sphere and cylinder models, J. Mech. Phys. Solids 27 (4) (1979) 315–330, https://doi.org/10.1016/0022-5096(79)90032-2.
[38] Z. Yousaf, N.F. Morrison, W.J. Parnell, Tensile properties of all-polymeric syntactic foam composites: Experimental characterization and mathematical modelling, Compos. Part B Eng. 231 (2022) 109556, https://doi.org/10.1016/j.compositesb.2021.109556.
[39] B. Paget, M. Zinet, P. Cassagnau, Syntactic foam under compressive stress: Comparison of modeling predictions and experimental measurements, J. Cell. Plast. 57 (3) (2021) 329–346, https://doi.org/10.1177/0021955X20943112.
[40] M. Thorpe, Deformation and buckling of isolated and interacting thin shells in an elastic medium, University of Manchester, 2016. PhD Thesis.
[41] M.E. Curd, N.F. Morrison, M.J.A. Smith, P. Gajjar, Z. Yousaf, W.J. Parnell, Geometrical and mechanical characterisation of hollow thermoplastic microspheres for syntactic foam applications, Compos. Part B Eng. 223 (2021) 108952, https://doi.org/10.1016/j.compositesb.2021.108952.
[42] Z. Hashin, Analysis of Composite Materials - a Survey, J. Appl. Mech. 50 (3) (1983) 481–505, https://doi.org/10.1115/1.3167081.
[43] C. Sullivan, A. Kaszynski, PyVista: 3D plotting and mesh analysis through a streamlined interface for the Visualization Toolkit (VTK), J. Open Source Softw. 4 (37) (2019) 1450, https://doi.org/10.21105/joss.01450.
[44] A. Shams, M. Aureli, M. Porfiri, Nonlinear buckling of a spherical shell embedded in an elastic medium with imperfect interface, Int. J. Solids Struct. 50 (14–15) (2013) 2310–2327, https://doi.org/10.1016/j.ijsolstr.2013.03.020.
[45] A. Shams, M. Porfiri, A generalized Vlasov-Jones foundation model for micromechanics studies of syntactic foams, Compos. Struct. 103 (2013) 168–178, https://doi.org/10.1016/j.compstruct.2013.04.020.
[46] A. Shams, M. Porfiri, Analysis of particle–matrix interfacial debonding using the proper generalized decomposition, Compos. Struct. 111 (2014) 602–618, https://doi.org/10.1016/j.compstruct.2014.01.037.
[47] Y. Gao, L. Ying, Z. Fan, Y. Wei, The failure behavior of syntactic foams as buoyancy materials for deepsea applications, Eur. J. Mech. - ASolids 105 (2024) 105256, https://doi.org/10.1016/j.euromechsol.2024.105256.
[48] W.T. Koiter, On the stability of elastic equilibrium, National Aeronautics and Space Administration (1970).
[49] J. Sieber, J.W. Hutchinson, J.M.T. Thompson, Nonlinear dynamics of spherical shells buckling under step pressure, Proc. R. Soc. Math. Phys. Eng. Sci. 475, 2223 (2019) 20180884, https://doi.org/10.1098/rspa.2018.0884.
[50] M.J.A. Smith, Z. Yousaf, P. Potluri, W.J. Parnell, Modelling hollow thermoplastic syntactic foams under high-strain compressive loading, Compos. Sci. Technol. 213 (2021) 108882, https://doi.org/10.1016/j.compscitech.2021.108882.
[51] Z. Hashin, The elastic moduli of heterogeneous materials, J. Appl. Mech. 29 (1) (1962) 143–150, https://doi.org/10.1115/1.3636446.
[52] K.J. Lee, R.A. Westmann, Elastic Properties of Hollow-Sphere-Reinforced Composites, J. Compos. Mater. 4 (2) (1970) 242–252, https://doi.org/10.1177/002199837000400209.
[53] L. Bardella, F. Genna, On the elastic behavior of syntactic foams, Int. J. Solids Struct. 38 (40–41) (2001) 7235–7260, https://doi.org/10.1016/S0020-7683(00)00228-6.
[54] Z. Hashin, Large isotropic elastic deformation of composites and porous media, Int. J. Solids Struct. 21 (7) (1985) 711–720, https://doi.org/10.1016/0020-7683(85)90074-5.
[55] G. deBotton, R. Bustamante, A. Dorfmann, Axisymmetric bifurcations of thick spherical shells under inflation and compression, Int. J. Solids Struct. 50 (2) (2013) 403–413, https://doi.org/10.1016/j.ijsolstr.2012.10.004.
[56] J. Schindelin, I. Arganda-Carreras, E. Frise, Fiji: an open-source platform for biological-image analysis, Nat. Methods 9 (2012) 676–682, https://doi.org/10.1038/nmeth.2019.
[57] D. Legland, I. Arganda-Carreras, P. Andrey, MorphoLibJ: integrated library and plugins for mathematical morphology with ImageJ, Bioinformatics 32 (22) (2016) 3532–3534, https://doi.org/10.1093/bioinformatics/btw413.